Photocatalytic robust solar energy reduction of dinitrogen to ammonia on ultrathin MoS$_2$

Songmei Sun [1], Xiaoman Li [1], Wenzhong Wang*, Ling Zhang, Xiang Sun

State Key Laboratory of High Performance Ceramics and Superfine Microstructure, Shanghai Institute of Ceramics, Chinese Academy of Sciences, Shanghai 200050, PR China

A B S T R A C T

The crux for solar N$_2$ reduction to ammonia is activating N$_2$ into its high-energy intermediate. Applying a simultaneous multi-electron reduction process could avoid intermediate generation and decrease the thermodynamic barrier. However, this process is extremely difficult from a kinetic view and experiments so far have not shown it is accessible. Here we show the first direct evidence of trion induced multi-electron N$_2$ reduction on ultrathin MoS$_2$. By applying light induced trions, N$_2$ molecular was activated and transformed into ammonia by a simultaneous six-electron reduction process, with a high ammonia synthesis rate of 325 μmol/g h without the assistant of any organic scavengers or co-catalyst. Bulk MoS$_2$ without trions did not exhibit any activity. This demonstrates multi-electron reduction may be realized in electron-rich semiconductors with high concentration of localized electrons such as trions. The methodology of simultaneous multi-electron reduction has wide implications for reactions beyond N$_2$ reduction and for materials beyond MoS$_2$.

© 2016 Elsevier B.V. All rights reserved.

1. Introduction

Heterogeneous catalytic conversion of N$_2$ to ammonia is one of the most important reactions in science and technology. It has played an important role in the development of modern industry and agriculture. Molecular N$_2$ is chemically and biologically inert due to its extremely strong, nonpolar triple bond (225 kcal/mol) as well as the large ionization potential [1–3]. The industrial ammonia synthesis typified by the Haber-Bosch process requires drastic reaction conditions of high pressures and temperatures [1,2,4,5], consuming 1–2% of the world's power source and generating more than 300 million tons of carbon dioxide [6]. Since the discovery of the first UV light induced N$_2$ reduction on TiO$_2$ based semiconductors by Schrauzer and Guth in 1977 [7], a great deal of efforts have been devoted to develop this green and economical ammonia synthesis routes that are capable of working under mild conditions.

Up to the present, various semiconductor photocatalysts, such as TiO$_2$, WO$_3$, Sm$_2$O$_3$·nH$_2$O/V$_2$O$_3$·nH$_2$O and diamond *etc.*, have been reported which could convert atmospheric N$_2$ to ammonia under UV or visible light irradiation [8–13]. However, the obtained ammonia concentrations by most of these photocatalysts were only

in the μM magnitude [8–13], which is far away from the practical demand. This dissatisfactory ammonia yield mainly arises from the difficult activation of insert N$_2$ on these catalysts, which is an uphill reaction process involved the generation of high-energy intermediate (N$_2$H, N$_2$H$_2$) [14–16]. For example, the reduction potential of the N$_2$H formation is as negative as −3.2 V vs. NHE via N$_2$ + H$^+$ + e$^-$ → N$_2$H. Through a two electron reduction process via N$_2$ + 2H$_2$O + 4H$^+$ + 2e$^-$ → 2NH$_3$OH$^+$, the reduction potential (-1.83 V vs. NHE) is still energetically impossible for most of traditional semiconductors (TiO$_2$, WO$_3$, Fe$_2$O$_3$, ZnO *etc.*) in the absence of any organic scavengers or precious-metal cocatalysts. Applying a multi-electron reduction process via N$_2$ + 5H$^+$ + 4e$^-$ → N$_2$H$_5^+$ (-0.23 V vs. NHE) or N$_2$ + 8H$^+$ + 6e$^-$ → 2NH$_4^+$ (0.274 V vs. NHE), in principle, may avoid the generation of high energy intermediates and decrease the thermodynamic barrier for ammonia production. However, this multi-electron photoreduction of N$_2$ is extremely difficult from a kinetic point and has not been reported accessible up to the present. Recently, Zhang et al. found localized electrons in oxygen vacancy could effectively active the adsorbed N$_2$ by electron donation and decrease the kinetic barrier for N$_2$ photoreduction [17]. Kitano et al. reported Ru-loaded electride [Ca$_{24}$Al$_{28}$O$_{64}$]$^{4+}$(e$^-$)$_4$(Ru/C12A7:e$^-$), which has high electron-donating power, works as an efficient catalyst for industrial ammonia synthesis [18]. These studies imply the unique advantage of electron-rich systems for N$_2$ activation and

reduction. Multi-electron N_2 reduction may be realized by increasing the concentration of localized electrons in a semiconductor.

To achieve this important goal, ultrathin transition metal dichalcogenides (TMDs) (e.g., MoS_2, $MoSe_2$, WS_2, WSe_2) with intriguing electrical, optical, and photovoltaic performances [19–22], were chosen as model materials. It has been reported the photoexcited electron-hole pairs in ultrathin TMDs could form tightly bound excitons [23–27]. Gedik et al. proved these tightly bound excitons can capture additional electrons to form charged excitons (such as trions) which possess exceptionally high dissociation energies (20–50 meV) [28]. These charged excitons with more than two electron in one bound state may act as electron-rich species to facilitate multi-electron reduction process of molecular N_2. Although TMDs have been widely used as electrocatalytic material for hydrogen evolution [29–31], the influence and implications of charged excitons for catalytic applications have not been explored thus far. Herein, we report the first experimental confirmation of photocatalytic N_2 reduction to ammonia by charged excitons on ultrathin MoS_2. The effect of charged excitons on the optical, optoelectronic, and electrochemical properties that significantly influence the photocatalytic N_2 reduction performance were discussed detailed in this manuscript.

2. Experimental section

2.1. Chemicals

All the chemical reagents were of analytical purity and were used as received from Shanghai Chemical Company without further purification.

2.2. Preparation

Hydrothermal MoS_2 was prepared by a previously reported method [32]. Typically, 7 mmol sodium molybdate dihydrate ($Na_2MoO_4 \cdot 2H_2O$) and 35 mmol thiourea (Mo:S = 1:5) were dissolved in 40 mL distilled water under vigorous stirring to form a homogeneous solution, then the pH was adjusted to less than 1 with 2 M HCl. After being stirred for 30 min, the solution was transferred into a 45 mL Teflon-lined stainless steel autoclave, maintained at 200 °C for 24 h and allowed to cool down to room temperature naturally. The obtained products were collected by centrifugation, washed with distilled water and ethanol, and dried at 60 °C about 12 h.

Sonicated ultrathin MoS_2 was prepared by ultrasonic treatment of the hydrothermal MoS_2 in water for 12 h. The obtained dispersion was centrifuged at a speed of 7000 rpm for 10 min. The top suspension was collected and freeze-drying to obtain the final sonicated ultrathin MoS_2.
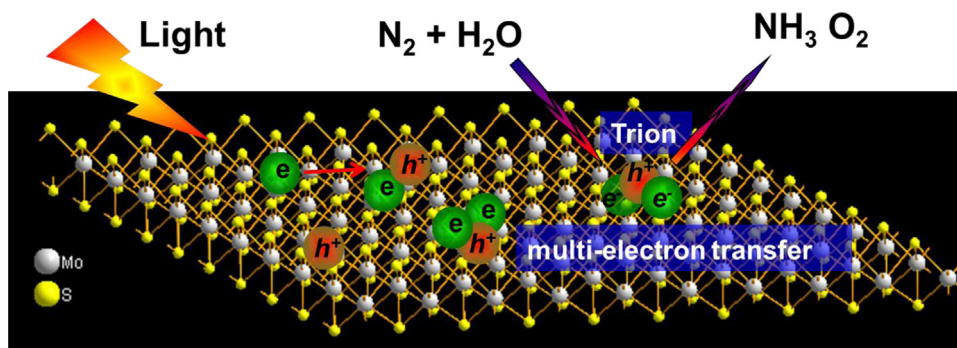
2.3. Characterization

The purity and the crystallinity of the as-prepared samples were characterized by powder X-ray diffraction (XRD) on a Japan Rigaku Rotaflex diffractometer using Cu Kα radiation while the voltage and electric current were held at 40 kV and 100 mA. The transmission electron microscope (TEM) analyses were performed by a JEOL JEM- 2100 F field emission electron microscope. UV–vis diffuse reflectance spectra (DRS) of the samples were measured using a Hitachi UV-3010PC UV–vis spectrophotometer. The photoluminescence (PL) spectra were measured with a Hitachi F4600 fluorescence spectrophotometer (excitation wavelength = 340 nm). Fourier transform infrared (FTIR) spectrum of concentrated ammonia product was performed with a spectrophotometer (Nicolet 380, Thermo, USA). Ion chromatography was measured using THERMO FISHER ICS-2100 Ion Chromatography System. Inductively coupled plasma-atomic emission spectrometry (ICP-AES) was performed on Agilent 725.

2.4. Photocatalytic test

Simulated solar light induced N_2 reduction experiments were performed under a 500 W Xe lamp located approximately 10 cm from the sample. Visible light was provided under this Xe lamp with a 420 nm cutoff filter. The reaction cell was made of Pyrex glass with a quartz window on top. For the atmospheric N_2 fixation, 0.015 g of the as-prepared photocatalyst powder was dispersed in 200 mL deionized water and then stirring under the simulated solar light irradiation. For ^{15}N isotopic labelling experiment, the reaction cell was enclosed by a quartz window on top. N_2 (20% $^{15}N_2$, 80% $^{14}N_2$) gas was slowly bubbled through the reaction vessel, which contained 200 mL deionized water until that was saturated. Then the reaction vessel was sealed and irradiated under the simulated solar light irradiation. During the photocatalytic tests, the temperature of the reaction vessel was maintained at 25 °C by providing a flow of cooling water. The concentration of ammonia in the reactor solution was measured using the indophenol blue method. The amount of evolved O_2 was determined by using online gas chromatography.

2.5. Electrochemical measurements

Electrochemical measurements were performed on a CHI 660D electrochemical workstation (Shanghai Chenhua, China) using a standard three-electrode cell with a working electrode, a platinum wire as counter electrode, and a standard saturated calomel electrode (SCE) in saturated KCl as reference electrode. The working electrodes were prepared by dip-coating: Briefly, 5 mg of photocatalyst was suspended in 0.1 mL of ethanol in the presence of 1% Nafion to produce slurry, which was then dip-coated onto a 2 cm × 1.5 cm FTO glass electrode and drying at 25 °C.

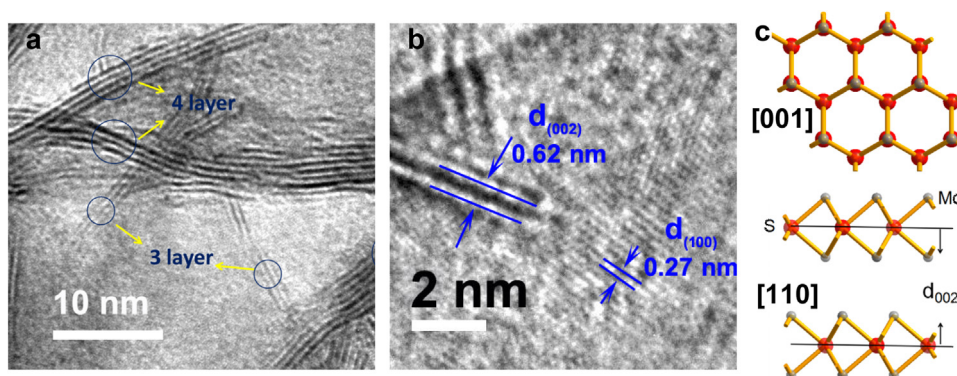**Scheme 1.** Schematic illustration of the trion induced multi-electron N_2 reduction process.

Fig. 1. (a) TEM and (b) HRTEM image of sonicated ultrathin MoS$_2$. (c) Schematic illustration of the crystal structure of hexagonal MoS$_2$ along [001] and [110] directions.

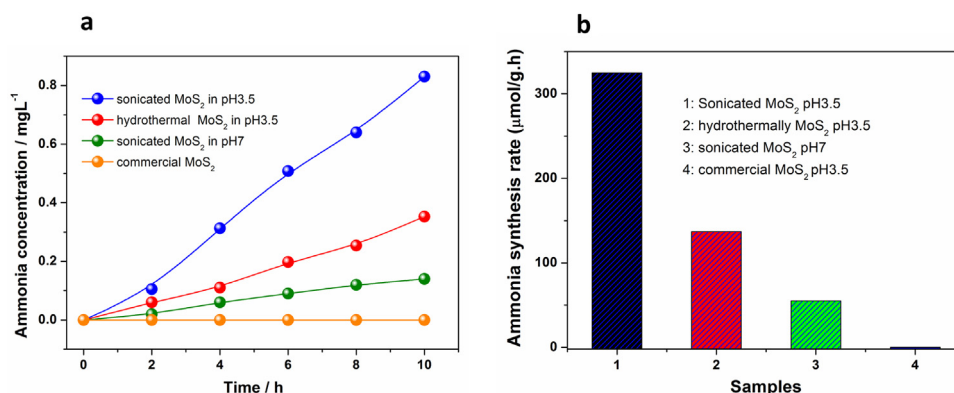**Fig. 2.** N$_2$ reduction and ammonia production efficiency of the as-prepared MoS$_2$ samples under different conditions. (a) Obtained ammonia concentration at different reaction time. (b) The corresponding ammonia synthesis rate.

2.6. Calculation of electron transfer number

For an adsorption-controlled and irreversible electrode process, according to Laviron [33], Ep is defined by the following equation:

$$Ep = E^0 + (RT/anF)ln\left(RTK^0/anF\right)\left(RTF/anF\right)\ln v$$

where a is transfer coefficient, k^0 is standard rate constant of the reaction, n is electron transfer number involved in the rate-determining step, v is scan rate(mV/S), and E^0 is formal potential. Other symbols have their usual meanings. For an irreversible electrode process, a $\approx$ 0.5.

3. Results and discussion

Fig. 1a shows the TEM image of the sonicated ultrathin MoS$_2$, which exhibits a lamellar morphology with 3~5 layers of S-Mo-S. The ultrathin structure was further confirmed by an HRTEM image. As shown in Fig. 1b, the interplanar spacing of 0.62 nm and 0.27 nm were clearly observed, which is consistent with the d spacing of (002) and (100) planes of hexagonal MoS$_2$, respectively. The schematic crystal structure of hexagonal MoS$_2$ in Fig. 1c further illustrates the lattice structure on (001) plane and the S-Mo-S layered structure along [001] and [110] directions. XRD pattern of the sonicated ultrathin MoS$_2$ indicates its high crystallinity and purity (Fig. S1). All of the diffraction peaks agree well with the standard pattern of hexagonal MoS$_2$ (JCPDS card No. 75-1539). The widened diffraction peaks were ascribed to the ultrathin thickness which is about 3.5 nm determined by calculating the full width at half

maximum (FWHM) value of the (002) diffraction peak based on the Scherrer equation. ICP analysis indicates the stoichiometry ratio of Mo: S in sonicated ultrathin MoS$_2$ is 1: 1.75, indicating a large amount of S vacancies may exist in the ultrathin structure. Without the ultrasonic treatment, the thickness of the hydrothermally synthesized MoS$_2$ nanosheet was mainly around 9–14 layers of S-Mo-S (as shown in Fig. S2).

To investigate the photocatalytic N$_2$ reduction properties of the prepared MoS$_2$ samples, 15 mg of the as-prepared powder sample was dispersed in 200 mL of deionized water in an open Pyrex cell equipped with a circulating water cooling system to main the reaction temperature at 25 °C. Before that, the ultrathin MoS$_2$ samples were washed with dilute hydrochloric acid (HCl) many times to eliminate the residual NH$_4^+$ which may be brought on in the synthetic process. During this process, the adsorbed NH$_4^+$ on the MoS$_2$ sample was replaced by H$^+$ via cation exchange. After the HCl washing, no residual NH$_4^+$ was detected in the reaction solution and the S^{2-} in the reaction solution was decreased to 1.1 μmol/L by ion chromatography. The reaction mixture was then irradiated under a 500 W Xenon arc lamp. During this process, the atmospheric N$_2$ in the reaction system was reduced into NH$_4^+$ by the ultrathin MoS$_2$ photocatalyst.

Fig. 2a shows the obtained ammonia concentration for various MoS$_2$ samples at different reaction conditions. Control experiments showed that NH$_4^+$ cannot be detected in the absence of MoS$_2$ catalyst or solar light irradiation. In contrast, simulated solar light irradiation resulted in continuous ammonia production from pure water by the as-prepared ultrathin MoS$_2$ samples. The generated ammonia concentration by the sonicated ultrathin MoS$_2$ sample is about 0.14 mg/L within 10 h in pure water. In an acidic reaction
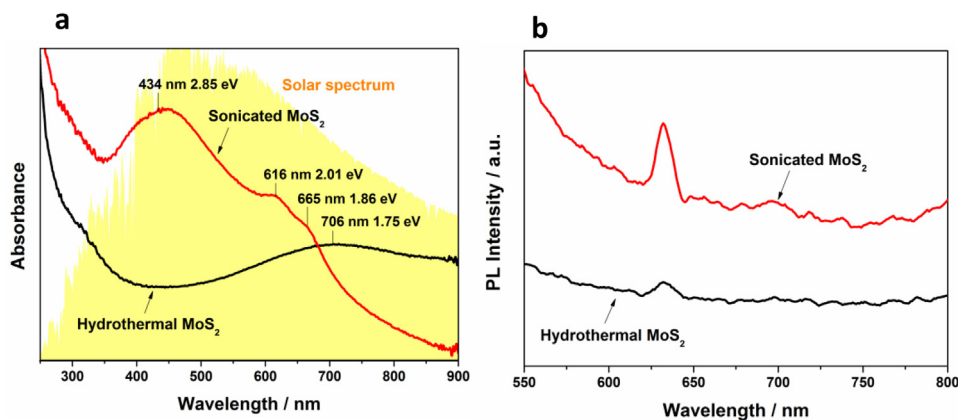
Fig. 3. Optical properties of the as-prepared MoS_2 samples. (a) UV−vis absorption spectra of the as-prepared MoS_2 samples dispersed in pure water. (b) Photoluminescent spectra of the as-prepared MoS_2 samples excited at 420 nm at room temperature.
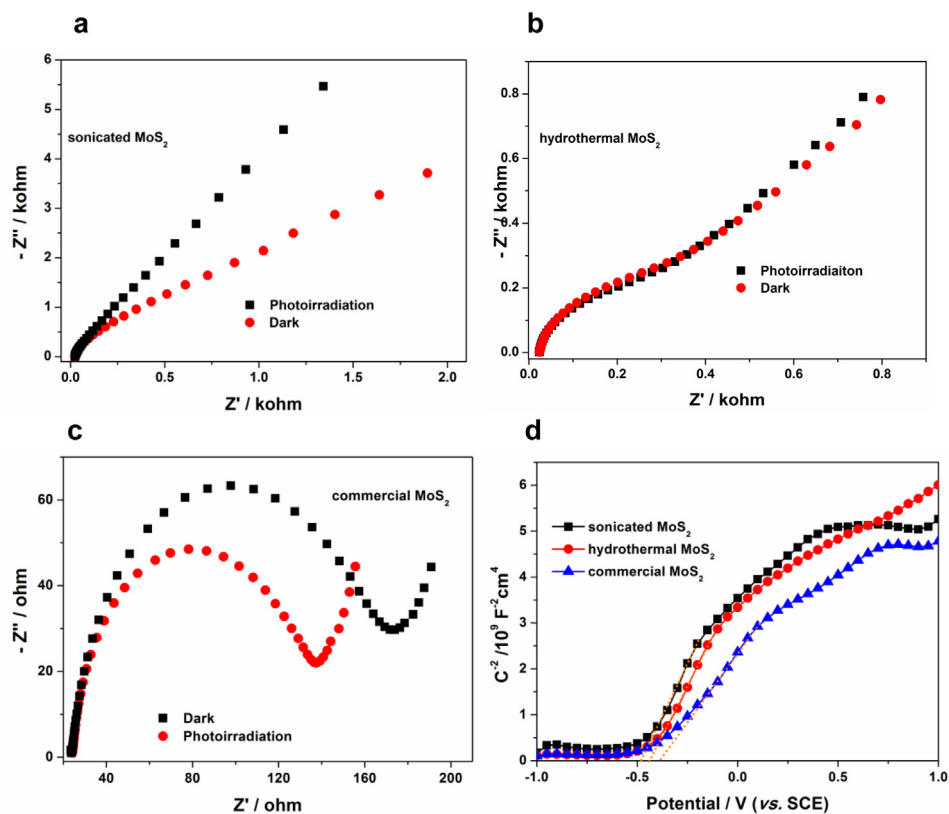

Fig. 4. Electrochemical impedance spectra (EIS) of sonicated ultrathin MoS_2 (a), hydrothermal MoS_2 (b) and commercial MoS_2 (c). (d) Mott−Schottky plots of the synthetic MoS_2 samples and commercial MoS_2.

solution (pH 3.5) which could provide excess protons to decrease the kinetic barrier for N_2 reduction, the generated ammonia concentration was increased to 0.83 mg/L by the sonicated ultrathin MoS_2 sample within 10 h, with a high ammonia synthesis rate of about 325 μmol/g (catalyst) h (Fig. 2b). Under the same conditions, the generated ammonia concentration by hydrothermally MoS_2 sample is 0.35 mg/L and no ammonia was detected by commercial bulk MoS_2, indicating the unique advantage of ultrathin MoS_2 for photocatalytic N_2 reduction to ammonia. When the photocatalytic N_2 reduction experiment was conducted under visible light irradiation ($\lambda > 420$ nm), the ultrathin MoS_2 samples also exhibited excellent photocatalytic activity. After 10 h of visible light irradiation, the obtained ammonia concentration for the sonicated and hydrothermal MoS_2 samples were 0.5 and 0.26 mg/L at pH 3.5 (as

shown in Fig. S3). Besides, the stability of the ultrathin MoS_2 was also investigated. After ten consecutive runs for the N_2 photoreduction experiment, the photocatalytic performance of the sonicated ultrathin MoS_2 was well-maintained and a total of 1.6 mg NH_4^+ was produced after 100 h. The XRD pattern (Fig. S4) and the UV–vis absorption spectrum (Fig. S5) of the spent ultrathin MoS_2 photocatalyst are almost the same as that of the initial MoS_2 sample, indicating the high stability of ultrathin MoS_2. The turnover number under this condition is 1.22, indicating the ammonia generation on MoS_2 surface is catalytic. Besides, a considerable amount of O_2 generation was observed during the photocatalytic ammonia synthesis process when the N_2 reduction experiment was conducted in a closed reaction system, indicating water may act as the sacrificial electron donor of photogenerated holes for ammonia generation.

To further confirm that the NH_4^+ detected comes from N_2 reduction, we conducted an isotopic labelling study using gaseous N_2 which contains 20 vol% $^{15}N_2$ as the purge gas. Infrared spectroscopy was used to characterize the NH_4^+ product. As shown in Fig. S6, besides the $^{14}NH_4^+$ which has an infrared absorption peak around $1400\,cm^{-1}$, $^{15}NH_4^+$ was also observed on the infrared spectrum with an adsorption peak around $1351\,cm^{-1}$ which is in good agreement with the value estimated according to the isotope effect (that is, $1400\,cm^{-1} \times (14/15)^{1/2} = 1352\,cm^{-1}$). This isotope labelling study confirmed that the NH_4^+ detected in our experiments originated from photocatalytic N_2 reduction and not from other sources.

Optical properties were studied to investigate the origin of the solar light induced N_2 photoreduction property of the ultrathin MoS_2 samples. The UV–vis absorption spectrum of the sonicated MoS_2 sample (Fig. 3a) shows the well-known A and B excitonic absorption bands at 665 nm (1.86 eV) and 616 nm (2.01 eV) [34,35]. These two absorption bands have been well established to be the direct excitonic transitions at the K point of the Brillouin zone in monolayer and few-layer MoS_2. In addition, an intense absorption band centered at 434 nm (2.85 eV) was also clearly observed. This is a feature absorption that is universal to monolayer TMDs and associated with Van Hove singularities in the density of states [36]. Different from the sonicated ultrathin MoS_2, the hydrothermal MoS_2 only displays one broad absorption band centered at 706 nm that may be attributed to the mixed optical absorption by the direct and indirect band transitions in few-layer and thicker MoS_2. The hydrothermal and the sonicated MoS_2 samples exhibit the similar photoluminescence (PL) spectrum around ~633 nm (Fig. 3b), corresponding to a band gap at 1.95 eV. However, the PL intensity of the sonicated MoS_2 is much stronger than that of the hydrothermal MoS_2 sample. A previous study by Mark et al. has demonstrated the PL around 1.9 eV was originated from the relaxation of direct excitons in monolayer MoS_2 [35]. Both of the UV–vis absorption and PL spectrum indicate the larger amount of photo-generated excitons in the sonicated sample under the same conditions, which may play a vital role in improving the photocatalytic N_2 reduction performance.

Photoelectrochemical measurements on the as-prepared MoS_2 samples further revealed the origin of the solar light induced N_2 reduction property. Fig. 4a shows the electrochemical impedance spectra (EIS) of the sonicated ultrathin MoS_2 electrode under different conditions. It is obvious that the diameter of the semicircle loop on the EIS Nynquist plot is enlarged under light irradiation, indicating a much decreased electrical conduction under photoirradiation. Generally, the conductivity of a semiconductor electrode is increased under light irradiation because of the generation of photo-electrons. The abnormal negative photoconductivity of ultrathin MoS_2 was induced by the strong many-body interactions in ultrathin 2D system, where photoexcited electron-hole pairs join the excess free charges to form trions (bound states of two electrons and one hole) [37]. These charged excitons have an increased carrier effective mass, substantially diminishing the conductivity. The negative photoconductivity is also slightly observed in hydrothermal MoS_2 sample (Fig. 4b), and completely vanished in commercial MoS_2 (Fig. 4c). Combined with the above photocatalytic performance of different MoS_2 samples, it is obvious the photocatalytic N_2 reduction performance is closely related to their photoconductivity. Only the hydrothermal and sonicated MoS_2 which have negative photoconductivity exhibited the photocatalytic N_2 reduction activity. Besides, the sonicated ultrathin sample with a much enhanced photoreduction of conductivity possesses the highest photocatalytic activity. The commercial MoS_2 which has normal positive photoconductivity exhibited no N_2 photoreduction performance. Therefore, the variation of photoconductivity in different MoS_2 samples is synchronization with the variation of their photocatalytic activity to a certain extent. This indicates trions induced

negative photoconductivity may play an important role on the photocatalytic N_2 reduction performance of ultrathin MoS_2.

To investigate the possibility of trion-induced N_2 photoreduction by ultrathin MoS_2, thermodynamic process of N_2 reduction on various MoS_2 samples was firstly analyzed by electrochemical studies. Fig. 4d is Mott−Schottky spectra of different MoS_2 samples, which is usually used for the analysis of the flat band potential (E_{fb}) of semiconductor electrodes [38]. The positive slope of the plot indicates these MoS_2 samples are n-type semiconductor with electrons as the majority charge carriers. The E_{fb} values which were calculated from the intercept of the axis with potential value were at −0.49 V, −0.44 V and −0.38 V vs SCE for the sonicated, hydrothermal and commercial MoS_2 samples, respectively. For many n-type semiconductors, E_{fb} is considered to be about 0.1 V below the conduction band (E_{cb}) [39]. Based on this, the estimated E_{cb} values of the sonicated, hydrothermal and commercial MoS_2 samples were −0.35 V, −0.3 V and −0.24 V vs. NHE respectively. It is obvious the conduction band edge position for all of the MoS_2 samples is located below the thermodynamic reduction potentials of N_2/N_2H and N_2/NH_3OH^+, which indicates photogenerated electrons on MoS_2 are difficult to take part in the N_2 reduction reaction by one-electron or two-electron transfer process.

It is most likely N_2 reduction to ammonia occurs by a multi-electron transfer process on the MoS_2 surface, considering the lower reduction potentials of $N_2/N_2H_5^+$ and N_2/NH_3. However, multi-electron transfer process is extremely difficult from a kinetic view. Although it is thermodynamically accessible, commercial MoS_2 exhibited no catalytic activity for ammonia generation. This study indicates the excellent N_2 reduction performance of ultrathin MoS_2 may be ascribed to trions induced multi-electron transfer reduction process. Besides, the valence band edge potentials of the sonicated and hydrothermal ultrathin MoS_2 samples which estimated from the band gap and E_{cb} were calculated at 1.51 and 1.45 V vs. NHE respectively at pH 7. These potentials are energetically large enough for water oxidation (0.82 V vs. NHE) at pH 7.

To verify the possibility of multi-electron reduction process on ultrathin MoS_2, the electron transfer number upon N_2 reduction on the as-prepared different MoS_2 electrodes was studied by analyzing the variation of the reduction peak potential (E_p) along with the change of the scan rate (ν) in a photoelectrochemical measurement [33]. From the slope of the E_p-$\ln\nu$ curve, a six electron transfer process (n = 6.04, Fig. 5a) was qualified on the ultrathin MoS_2 electrode based on the analysis of its higher reduction peak around −1.17 V vs. SCE. Under the same conditions, the electron transfer number of commercial MoS_2 electrode is calculated to be 2.33 (Fig. 5b). As mentioned above, photogenerated electrons in MoS_2 is energetically impossible for N_2 reduction by two-electron transfer process. Therefore, without trions assistant multi-electron transfer process, commercial MoS_2 is inactive on N_2 photoredution.

Based on the above analysis, the mechanism for the photocatalytic N_2 reduction on ultrathin MoS_2 was illustrated in Scheme 1. As an n-type semiconductor, ultrathin MoS_2 possess lots of free electrons. Under solar light irradiation, these free electrons were attracted by the light generated excitons (electron-hole pairs) to form charged excitons (trions, as shown in Scheme 1). These charged excitons have multiple electrons in one bound state, which could contribute to multi-electron transfer reactions. First-principles calculations have indicated the valence band maximum and conduction band minimum both in bulk and single layer MoS_2 mainly consists of Mo 4d contributions [40]. Therefore, the photo-generated charged excitons were mainly located around the Mo sites. Due to the large amount of S vacancies in the ultrathin MoS_2, the N_2 molecules are most probably captured by these S vacancies and activated upon donating electrons from its bonding orbitals and accepting electrons to its three antibonding orbitals. From the crystal structure in Fig. 1c, it can be seen every S atom
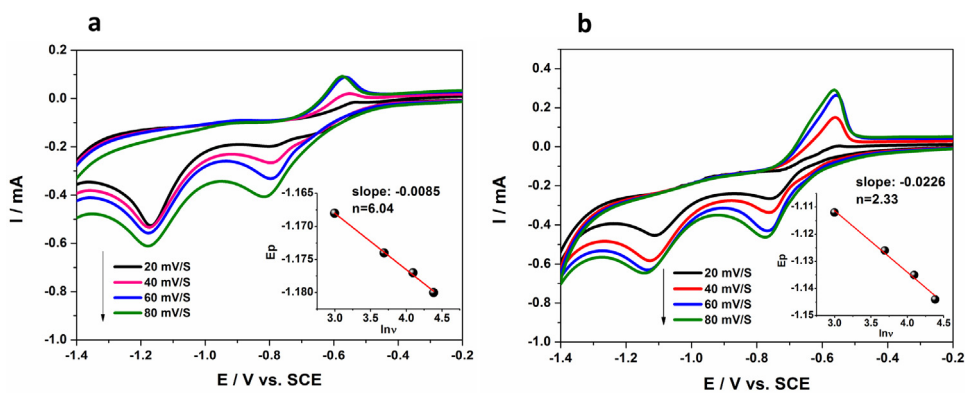
Fig. 5. Kinetic study of N_2 photoreduction on MoS_2 catalyst by photoelectrochemical measurements. (a) Cyclic voltammograms of sonicated ultrathin MoS_2 electrode. (b) Cyclic voltammograms of commercial MoS_2 electrode. The experiment was performed at different scan rates in N_2 saturated 0.5 M Na_2SO_4 (pH = 3.5) under room temperature (25 °C) and simulated sun light irradiation; Inset: the plot for the reduction peak potential (Ep) vs. lnν (scan rate).

connected with three Mo atoms. Therefore, the adsorbed N_2 molecules on the S vacancy are most likely surrounded by three Mo atoms. Under solar light irradiation, the photogenerated charged excitons on these Mo atoms may cooperate with the center-adsorbed N_2 molecule and resulted in a possible trions assistant six-electron reduction process. In our N_2 photoreduction experiment, only NH_4^+ was detected, although there are possibilities for the formation of other products such as N_2H_4 in N_2 reduction process. This photocatalytic performance data, therefore, further support our hypothetical interpretations of the N_2 reduction mechanism.

4. Conclusion

Simultaneous multi-electron reduction of N_2 was put forward to decrease the thermodynamic barrier for N_2 photoreduction to ammonia. Although this process is extremely difficult from a kinetic point, our study indicates it may be realized by electron-rich semiconductor photocatalyst which have high concentration of localized electrons such as trions. Ultrathin MoS_2 was synthesized as model material to verify trion induced simultaneous multi-electron photoreduction of N_2. Photoelectrochemical measurements proved trions in ultrathin MoS_2 was responsible for the photocatalytic N_2 reduction performance by simultaneous six-electron reduction process. The photocatalytic ammonia synthesis rate of ultrathin MoS_2 is up to 325 μmol/g h without the assistant of any organic scavengers or co-catalyst. Under the same conditions, the bulk MoS_2 without charged excitons did not exhibit any N_2 reduction activity. The methodology of simultaneous multi-electron reduction has wide implications for other multi-electron transfer reactions such as CO_2 photoreduction in electron-rich catalytic material beyond ultrathin MoS_2.

Acknowledgments

Appendix A. Supplementary data

Supplementary data associated with this article can be found, in the online version, at http://dx.doi.org/10.1016/j.apcatb.2016.07.025.

References

[1] J.A. Pool, E. Lobkovsky, P.J. Chirik, Nature 427 (2004) 527–530.
[2] J.W. Erisman, M.A. Sutton, J. Galloway, Z. Klimont, W. Winiwarter, Nat. Geosci. 1 (2008) 636–639.
[3] H. Tanaka, A. Sasada, T. Kouno, M. Yuki, Y. Miyake, H. Nakanishi, Y. Nishibayashi, K. Yoshizawa, J. Am. Chem. Soc. 133 (2011) 3498–3506.
[4] R. Schlögl, Angew. Chem. Int. Ed. 42 (2003) 2004–2008.
[5] T. Shima, S. Hu, G. Luo, X. Kang, Y. Luo, Z. Hou, Science 340 (2013) 1549–1552.
[6] Y. Tanabe, Y. Nishibayashi, Coordin. Chem. Rev. 257 (2013) 2551–2564.
[7] G.N. Schrauzer, T.D. Guth, J. Am. Chem. Soc. 99 (1977) 7189–7193.
[8] O. Rusina, A. Eremenko, G. Frank, H.P. Strunk, H. Kisch, Angew. Chem. Int. Ed. 40 (2001) 3993–3995.
[9] E. Endoh, J.K. Leland, A.J. Bard, J. Phys. Chem. 90 (1986) 6223–6226.
[10] J. Soria, J.C. Conesa, V. Augugliaro, L. Palmisano, M. Schiavello, A. Sclafani, J. Phys. Chem. 95 (1991) 274–282.
[11] O.P. Linnik, H. Kisch, Mendeleev Commun. 18 (2008) 10–11.
[12] D. Zhu, L. Zhang, R.E. Ruther, R.J. Hamers, Nat. Mater. 12 (2013) 836–841.
[13] K. Tennakone, C.T.K. Thaminimulla, W.C.B. Kiridena, Langmuir 9 (1993) 723–726.
[14] N. Bauer, J. Phys. Chem. 64 (1960) 833–837.
[15] T. Bazhenova, A. Shilov, Coord. Chem. Rev. 144 (1995) 69–145.
[16] C. Willis, R.A. Back, Can. J. Chem. 51 (1973) 3605–3619.
[17] H. Li, J. Shang, Z. Ai, L. Zhang, J. Am. Chem. Soc. 137 (2015) 6393–6399.
[18] M. Kitano, Y. Inoue, Y. Yamazaki, F. Hayashi, S. Kanbara, S. Matsuishi, T. Yokoyama, S.W. Kim, M. Hara, H. Hosono, Nat. Chem. 4 (2012) 934–940.
[19] S. Wu, J.S. Ross, G.B. Liu, G. Aivazian, A. Jones, Z. Fei, W. Zhu, D. Xiao, W. Yao, D. Cobden, X. Xu, Nat. Phys. 9 (2013) 149–153.
[20] K.F. Mak, K. He, J. Shan, T.F. Heinz, Nat. Nanotechnol. 7 (2012) 494–498.
[21] Q. Wang, K. Kalantar-Zadeh, A. Kis, J.N. Coleman, M.S. Strano, Nat. Nanotechnol. 7 (2012) 699–712.
[22] J. Shi, D. Ma, G.F. Han, Y. Zhang, Q. Ji, T. Gao, J. Sun, X. Song, C. Li, Y. Zhang, X.Y. Lang, Y. Zhang, Z. Liu, ACS Nano 8 (2014) 10196–10204.
[23] D.Y. Qiu, F.H. da Jornada, S.G. Louie, Phys. Rev. Lett. 111 (2013) 216805.
[24] K. He, N. Kumar, L. Zhao, Z. Wang, K.F. Mak, H. Zhao, J. Shan, Phys. Rev. Lett. 113 (2014) 026803.
[25] A. Chernikov, T.C. Berkelbach, H.M. Hill, A. Rigosi, Y. Li, O.B. Aslan, D.R. Reichman, M.S. Hybertsen, T.F. Heinz, Phys. Rev. Lett. 113 (2014) 076802.
[26] Z. Ye, T. Cao, K. O'Brien, H. Zhu, X. Yin, Y. Wang, S.G. Louie, X. Zhang, Nature 513 (2014) 214–218.
[27] M.M. Ugeda, A.J. Bradley, S.F. Shi, F.H. da Jornada, Y. Zhang, D.Y. Qiu, W. Ruan, S.K. Mo, Z. Hussain, Z.X. Shen, F. Wang, S.G. Louie, M.F. Crommie, Nature Mater. 13 (2014) 1091–1095.
[28] C.H. Lui, A.J. Frenzel, D.V. Pilon, Y.H. Lee, X. Ling, G.M. Akselrod, J. Kong, N. Gedik, Phys. Rev. Lett. 113 (2014) 166801.
[29] L. Cheng, W. Huang, Q. Gong, C. Liu, Z. Liu, Y. Li, H. Dai, Angew. Chem. Int. Ed. 53 (2014) 7860–7863.
[30] L. Tao, X. Duan, C. Wang, X. Duan, S. Wang, Chem. Commun. 51 (2015) 7470–7473.
[31] J. Xie, J. Zhang, S. Li, F. Grote, X. Zhang, H. Zhang, R. Wang, Y. Lei, B. Pan, Y. Xie, J. Am. Chem. Soc. 135 (2013) 17881–17888.
[32] J. Xie, H. Zhang, S. Li, R. Wang, X. Sun, M. Zhou, J. Zhou, X.W. Lou, Y. Xie, Adv. Mater. 25 (2013) 5807–5813.
[33] E. Laviron, J. Electroanal. Chem. Interfacial Electrochem. 52 (1974) 355–393.
[34] A. Splendiani, L. Sun, Y. Zhang, T. Li, J. Kim, C.Y. Chim, G. Galli, F. Wang, Nano Lett. 10 (2010) 1271–1275.
[35] K.F. Mak, C. Lee, J. Hone, J. Shan, T.F. Heinz, Phys. Rev. Lett. 105 (2010) 136805.
[36] L. Britnell, R.M. Ribeiro, A. Eckmann, R. Jalil, B.D. Belle, A. Mishchenko, Y.J. Kim, R.V. Gorbachev, T. Georgiou, S.V. Morozov, A.N. Grigorenko, A.K. Geim, C. Casiraghi, A.H. Castro Neto, K.S. Novoselov, Science 340 (2013) 1311–1314.

[37] K.F. Mak, K. He, C. Lee, G.H. Lee, J. Hone, T.F. Heinz, J. Shan, Nature Mater. 12 (*2013*) 207–211.

[38] A. Watanabe, H. Kozuka, J. Phys. Chem. B 107 (2003) 12713–12720.

[39] Y. Matsumoto, J. Solid State Chem. 126 (1996) 227–234.

[40] E.S. Kadantsev, P. Hawrylak, Solid State Commun. 152 (2012) 909–913.